Simulation of Rotating Asymmetric Sideways Forces during Vertical Displacement Events in CFETR

Changzhi Jiang(蒋长智), Shunwen Wang(王顺文), Zhenyu Zhou(周振宇), Di Hu(胡地)*, Bo Li(李博)*, and JOREK team†

School of Physics, Beihang University, Beijing 100191, China

(Received 16 April 2024; accepted manuscript online 5 July 2024)

Tokamak plasmas with elongated cross sections are susceptible to vertical displacement events (VDEs), which can damage the first wall via heat flux or electromagnetic (EM) forces. We present a 3D nonlinear reduced magnetohydrodynamic (MHD) simulation of CFETR plasma during a cold VDE following the thermal quench, focusing on the relationship among the EM force, plasma displacement, and the $n = 1$ mode. The dominant mode, identified as $m/n = 2/1$, becomes destabilized when most of the current is contracted within the $q = 2$ surface. The displacement of the plasma current centroid is less than that of the magnetic axis due to the presence of SOL current in the open field line region. Hence, the symmetric component of the induced vacuum vessel current is significantly mitigated. The direction of the sideways force keeps a constant phase approximately compared to the asymmetric component of the vacuum vessel current and the SOL current, which in turn keep in-phase with the dominant 2/1 mode. Their amplitudes are also closely associated with the growth of the dominant mode. These findings provide insights into potential methods for controlling the phase and amplitude of sideways forces during VDEs in the future.

DOI: 10.1088/0256-307X/41/8/085201

The IPB98(y,2) scaling law of ITER[1] gives the thermal energy confinement time $\tau_{\mathrm{th,\,98y2}} = 0.0562 I_{\mathrm{p}}^{0.93} B_{\mathrm{t}}^{0.15} n_{19}^{0.41} P_{\mathrm{L}}^{-0.69} R^{1.97} \varepsilon^{0.58} \kappa_a^{0.78} M^{0.19}$, where the effective elongation is defined as $\kappa_a = S_{\mathrm{c}}/\pi a^2$ with S_{c} being the cross section. This scaling law suggests that the elongated cross section can greatly improve the confinement time. However, the large elongation makes the plasma susceptible to vertical instability and undergoes vertical displacement events (VDEs) during disruptions. Electromagnetic (EM) load and heat deposition during VDEs may cause severe damage to the device.[2] The elongation ratio of the China Fusion Engineering Test Reactor (CFETR) is as high as 2.0,[3] and therefore it is essential to study the consequences of VDEs in CFETR plasma.

There have been intensive theoretical[4–8] and numerical[7,9–17] investigations into the vertical and sideways force experienced by the wall. The sideways wall force during VDE in JET was estimated to be several mega Newtons[4,18] and reproduced by M3D simulation.[19] In JET experiments, the asymmetries and rotation of plasma currents are found to lead to the rotation of sideways force and might cause dynamic amplification by the resonance of machine.[20] Previous simulation of the CFETR plasma shows that the magnitude of the wall force does not show obvious differences between hot and cold VDEs, but they have different time responses.[21] The sideways component of the wall force is proportional to the toroidal magnetic field and plasma current.[22] The 2D simulations conclude that injection of impurities accelerates the quench of the plasma current before it moves to the first wall and forms the open-field-line current.[23] For mitigated 3D ITER simulations,[10] the sideways force is found to be small because the fast current decay and the asymmetric modes can only reach small magnitudes. Unmitigated 3D simulations by multiple codes show that the total sideways force direction is not obviously correlated with the $n = 1$ mode, although it rises with the $n = 1$ magnetic energy.[24] Here n is the toroidal mode number.

In this work, we examine the force distribution on the vacuum vessel and analyze the phase correlation between the perturbed plasma mode structure for the dominant $n = 1$ mode and the rotating sideways forces acting on the vacuum vessel and the scrape-off-layer (SOL) current. Our analysis demonstrates that these forces are aligned in both phase and amplitude. Previous studies confirmed that in the 3D case, the most unstable mode is the $n = 1$ mode, while the growth rate of higher-order modes are orders of magnitude lower.[10,25] Hence, we only consider the $n = 0$ and the $n = 1$ Fourier harmonics in this simulation. The reduced nonlinear magnetohydrodynamic (MHD) code JOREK[26] is used to simulate the cold VDE during the plasma disruption. The STARWALL[27,28] code is used to model the symmetric vacuum vessel, poloidal field coils, and central solenoid coil in CFETR. The thermal quench (TQ) is mimicked by artificially increasing the heat diffusion until the plasma is cooled down. The plasma displacement and the $n = 1$ mode response to the plasma scraping-off are simulated, with a focus on the vacuum vessel current and the associated EM force.

*Corresponding authors. Email: hudi2@buaa.edu.cn; plasma@buaa.edu.cn
†See Hoelzl *et al.* 2021 for the JOREK team: https://doi.org/10.1088/1741-4326/abf99f

We use Braginskii electron and ion parallel heat conduction with an upper limit, mimicking the flux-limited heat flux in a free-streaming plasma. This upper limit corresponds to the Braginskii electron thermal conduction value at $T = 3.1\,\mathrm{keV}$, beyond which the thermal conduction will not increase anymore. The perpendicular heat conductivity is chosen as $\kappa_\perp = 4.10 \times 10^{-6}\,\mathrm{kg\cdot m^{-1}\cdot s^{-1}}$. The perpendicular diffusivity is selected as $D_\perp = 7.29\,\mathrm{m^2\cdot s^{-1}}$. In addition, the Spitzer resistivity is used, thus the parallel resistivity $\eta = 8.10 \times 10^{-11}\,\Omega\cdot\mathrm{m}$ initially at the plasma core, the corresponding Lundquist number $S = 6.2 \times 10^7$. After the TQ, the resistivity is increased according to the Spitzer temperature dependence.

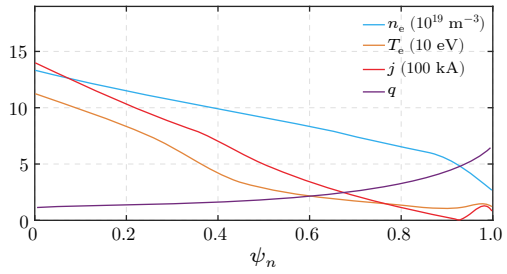

Fig. 1. Profiles of electron density n_e, electron temperature T_e, current density j, and safety factor q, averaged over poloidal magnetic flux surfaces at $t = 5.15\,\mathrm{ms}$ after the TQ and before significant vertical displacement.

The initial equilibrium total plasma current $I_\mathrm{p} = 11.2\,\mathrm{MA}$, the magnetic field $B = 6.53\,\mathrm{T}$, the initial magnetic axis location $R = 7.8\,\mathrm{m}$, $Z = 0.78\,\mathrm{m}$. As mentioned above, the TQ is mimicked by manually increasing the perpendicular heat conductivity $\kappa_\perp = 4.10 \times 10^{-2}\,\mathrm{kg\cdot m^{-1}\cdot s^{-1}}$. The TQ is carried out in 2D and is stopped when the electron temperature at the magnetic axis drops to around 100 eV at $t = 0.46\,\mathrm{ms}$. Then, the perpendicular heat conductivity is adjusted to the default value. During the TQ phase, the plasma equilibrium experiences a rapid change in its Shafranov shift due to the artificially imposed large heat transport and the consequent sudden pressure change. As a result, the plasma experiences several violent shakes during the 2D TQ process, which gradually subside as the TQ phase concludes. Subsequently, the current quench (CQ) phase begins, and vertical displacement manifests at $t = 18.2\,\mathrm{ms}$. At this time, we switch from the 2D simulation to the 3D one. Figure 1 shows the profile after the TQ and before significant vertical displacement at $t = 5.15\,\mathrm{ms}$. We did not consider the current flattening as a result of the nonlinear $\boldsymbol{v}\times\boldsymbol{B}$ induced hyper-resistivity during the process;[29] thus the current remains peaked in the core. We do not expect this to impact our result significantly.

The grid of the vacuum vessel (VV) utilized for STARWALL response and the configuration of poloidal field and central solenoid coils are shown in Fig. 2. The coupled STARWALL code constructs the response matrix of the resistive VV, which is used in the JOREK free boundary simulation. The VV resistivity $\eta_\mathrm{vv} = 1.32 \times 10^{-5}\,\Omega\mathrm{m}$, thus the resistive VV magnetic penetration time $\tau_\mathrm{vv} = 0.21\,\mathrm{s}$. We choose our JOREK simulation domain to correspond more or less to the shape of the first wall (i.e., the plasma-facing wall) in this study. The ratio of τ_vv to the CQ time, τ_CQ, is of general interest as it determines the specific q surface into which the plasma current channel contracts.[30] This contraction significantly influences the dominant tearing/resistive instability modes in the plasma, where the amplitude of these modes dictates the magnitude of the sideways force. As will be illustrated later, while the current in the VV begins to decay, the total plasma current changes only slightly. Therefore, in our simulation, τ_CQ greatly exceeds τ_vv.

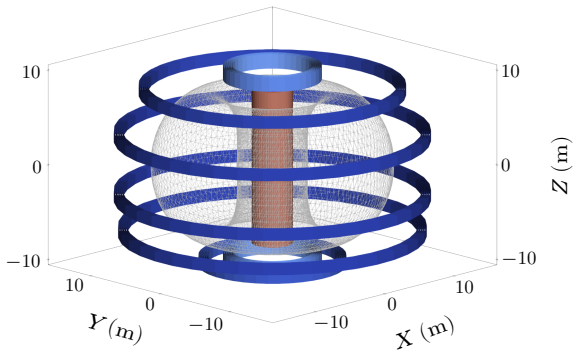

Fig. 2. STARWALL elements (gray mesh grid) and coil configuration in the simulation of CFETR. The poloidal field coils are blue and the central solenoid is red.

As is shown in Fig. 3(a), the displacement of the current centroid (the orange trajectory) is far less than that of the magnetic axis (the green trajectory) because the induced open-field-line SOL currents outside the last closed flux surface (LCFS) make the current centroid and magnetic axis spatially non-coincident. In Fig. 3(c), the SOL currents are induced soon after the TQ starts due to the rapid decay of the plasma current inside the LCFS. These SOL currents persist throughout the entire VDE, as shown in Fig. 3(d). Since the displacement of the current centroid is a primary factor driving the induced current in the VV, the existence of the SOL current mitigates the current induction in the VV, thereby reducing the associated VV force. This is consistent with previous reports,[23] which show that the existence of the SOL current is shown to help mitigate the induced current in the VV. However, such SOL current will experience the EM force, which will then act on the simulation boundary due to the zero perpendicular velocity boundary condition.

The vertical displacement results in scraping-off and subsequent edge cooling of the plasma, which destabilizes the $m/n = 2/1$ tearing/resistive kink mode. Here m is the poloidal mode number. As shown in Fig. 3(b), most of the plasma current is concentrated within the $q = 2$ surface, leading to the dominance of the 2/1 instability. Outside the $q = 2$ surface, the magnetic field lines become completely stochastic, leading to enhanced edge cooling and facilitating the current contraction. A noteworthy feature is that the current channel stops further contraction once the 2/1 mode becomes significant. Indeed, as will be seen later, the current fraction within the $q = 2$ surface even begins to decay somewhat. The absence of further current contraction contributes to the saturation of the 2/1 mode

amplitude, thereby preventing the emergence of a more violent 1/1 kink mode. This saturation of the instability mode amplitude, in turn, contributes to the smallness of sideways forces in our simulations.

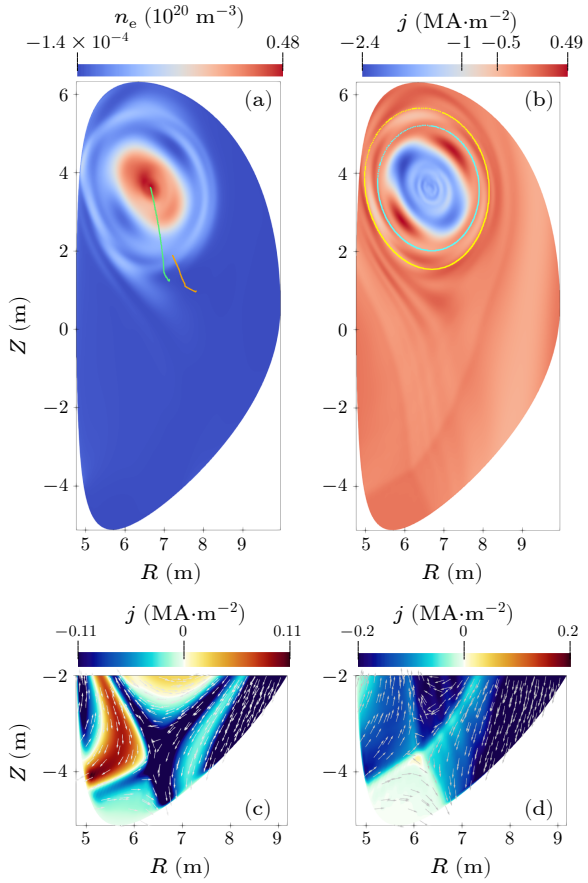

Fig. 3. At $t = 151.01$ ms and in the $\phi = 0$ plane: (a) The magnetic axis (green) and current centroid (orange) trajectories overlap on the electron density profile. (b) The $q = 2, 3$ surfaces, shown by cyan and yellow lines, overlap on the current density poloidal profile. The sign of the current density is determined by its direction. The current density poloidal profile slice in the divertor region before the vertical displacement ($t = 1.32$ ms) is shown in (c), and at the end of the vertical displacement ($t = 124.9$ ms) in (d). The arrows in (c) and (d) indicate the directions of the SOL current projected in the poloidal plane.

The simulation area for the plasma, shown in Fig. 3, is bounded by the first wall, which is depicted in Fig. 4. The MHD simulation boundary for the plasma in JOREK is magnetically transparent. All electromagnetic responses originating from the VV are calculated by STARWALL and then fed back to the JOREK simulation boundary (hereafter referred to as the simulation boundary). The VV is modeled as a resistive thin surface, as illustrated in Fig. 4. A vacuum exists between the VV and the simulation boundary, which means that there is no shared current between the plasma and the VV. Consequently, the EM force acting on the wall is calculated separately: the EM force generated by the volume integrals of $\boldsymbol{J} \times \boldsymbol{B}$ on the VV reads

$$\boldsymbol{F}_{\rm vv} = \int_{\rm VV} \boldsymbol{J} \times \boldsymbol{B} dV, \tag{1}$$

and the EM force applied to the plasma reads

$$\boldsymbol{F}_{\rm pl} = \int_{\rm plasma} \boldsymbol{J} \times \boldsymbol{B} dV. \tag{2}$$

Due to numerical constraints, the simulation boundary condition sets the plasma velocity perpendicular to the boundary to zero, causing the plasma to decelerate near the boundary and generating an equivalent force acting on it. This is entirely an artificial effect, corresponding to the force of plasma-wall contact. In a more realistic scenario, this force would occur within the 'wet zone' where the plasma touches the wall. Since the plasma inertia is negligible [31] and the timescale of the VDE far exceeds that of inertia, the plasma must be in force equilibrium. The plasma pressure, which might affect the force balance, [32] is very low near the boundary region due to the low temperature, especially when compared with the EM force. Hence, the total EM force acting on the entire plasma, $F_{\rm pl}$, as expressed by Eq. (2), is balanced by the force exerted by the simulation boundary. Consequently, the total force exerting on the VV and the first wall is $\boldsymbol{F}_{\rm tot} = \boldsymbol{F}_{\rm vv} + \boldsymbol{F}_{\rm pl}$.

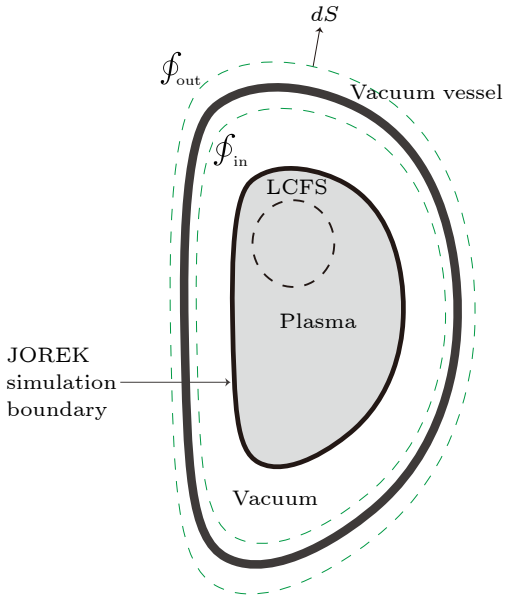

Fig. 4. The sketch illustrates the configuration of the simulation. The outermost black solid line represents the VV, which is a resistive thin surface. The inner black solid line represents the JOREK simulation boundary, corresponding to the shape of the first wall. The black dashed line represents the LCFS. The green dashed line inside or outside the VV represents the surface where the surface integration $\oint_{\rm in}$ or $\oint_{\rm out}$ is performed.

To simplify the calculations, $\boldsymbol{F}_{\rm vv}$ is determined using the following equation, which converts the volume integration into a surface integration: [31]

$$\boldsymbol{u} \cdot \boldsymbol{F}_{\rm vv} = F_{\rm out} - F_{\rm in}, \tag{3}$$

with

$$F_{\rm in/out} = \frac{1}{\mu_0} \oint_{\rm in/out} \left\{ (\boldsymbol{B} \cdot \boldsymbol{u}) \boldsymbol{B} - \frac{B^2}{2} \boldsymbol{u} \right\} \cdot d\boldsymbol{S}. \tag{4}$$

As shown in Fig. 4, $\oint_{\rm in}$ represents the surface integration over the surface near and inside the VV, which separates

the VV from the plasma simulation boundary and fully encloses the plasma. In contrast, $\oint_{\text{out}}$ represents the surface integration near and enclosing the VV, with the external poloidal field coils and the central solenoid remaining outside this surface. Further, $\boldsymbol{u}$ represents unit vectors pointing toward any specific direction. The directions of the surface elements $d\boldsymbol{S}$ are pointed outward; therefore, the inner VV surface integration equals the total EM force acting on the plasma, $F_{\text{in}} = F_{\text{pl}}$. The difference between inner and outer surface integrals equals the sum of EM loads on the VV generated by the cross product of induced VV current and the magnetic field which is generated by plasma and coil currents, $\boldsymbol{J}_{\text{vv}} \times \boldsymbol{B}_{\text{pl+coil}}$. The contribution from the VV current carried magnetic field vanishes after integration.

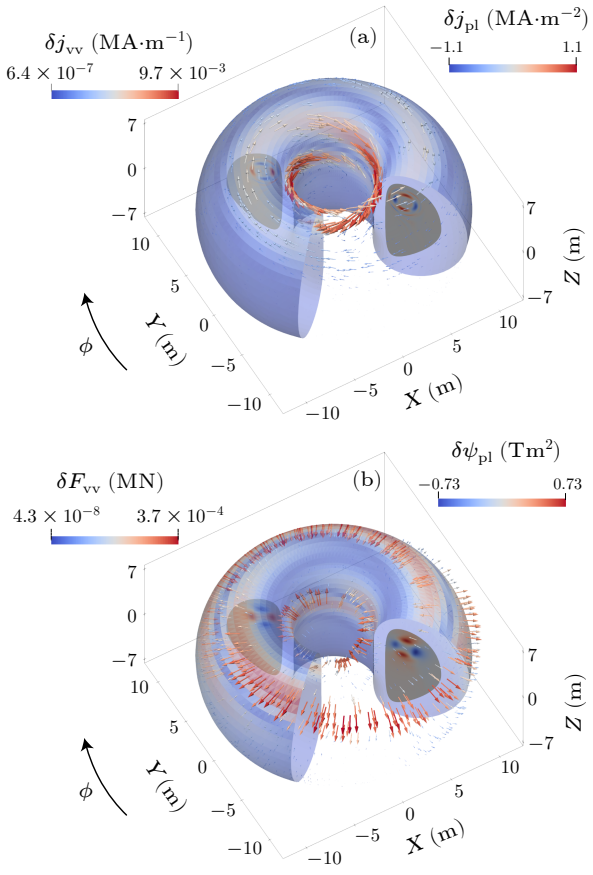

Fig. 5. (a) Spatial distribution of the asymmetric components of the VV currents. (b) Spatial distribution of the asymmetric components of $\boldsymbol{J} \times \boldsymbol{B}dV$ force on the VV at $t = 143.26$ ms. Length and color of the arrows denote the magnitudes of the surface current density and that of the VV forces. The plasma poloidal cross section of perturbed components of (a) plasma current δj_{pl} and (b) poloidal magnetic flux $\delta\psi$ are also shown in the corresponding toroidal locations ($\phi = 45°$ and $\phi = 225°$) for comparing the phase of plasma perturbation, asymmetric components of VV currents, and the VV forces. Here $\phi = 0$ corresponds to the positive half of the x-axis. Positive ϕ direction is clockwise.

The sideways force is found to be directly related to the growth of the asymmetric mode. The spatial distributions of asymmetric components of VV currents, VV forces, and perturbed plasma profile are shown in Fig. 5. The double helical structure of VV currents spatially correlates with the 2/1 current perturbation's helicity, as shown in Fig. 5(a). The asymmetric VV current is in the opposite direction compared to the plasma current perturbation, consistent with the fact that they are induced by the plasma current perturbation, which in turn are attributed to the distortion of the magnetic flux tube $\delta J = \xi \cdot \nabla J$, where ξ is the displacement of magnetic flux and ∇J is the averaged current densities gradient. Further, the spatial distribution of the asymmetric component of the VV force is shown in Fig. 5(b). Here, the force per element is calculated by the cross product of the surface VV current density and the magnetic field $\boldsymbol{\sigma} \times \boldsymbol{B}dS$, then subtracting the axisymmetric component. Here $\boldsymbol{\sigma}$ is the line current density within the VV. It can be seen that despite the induced current density being more pronounced in the high field side (HFS), the low field side (LFS) elements' area S is greater than the HFS; thus the forces on LFS elements are larger compared with that on the HFS. The directions of asymmetric components of VV forces are almost horizontal because the main contribution is from the poloidal VV currents (only contributed by the asymmetric VV currents) and the toroidal magnetic field.

A more detailed analysis of the correlation between the phase of the dominant mode, the VV currents, and the VV forces is shown in Fig. 6. The vertical component of $\boldsymbol{F}_{\text{pl}}$ emerges on the order of MNs after the mimic TQ due to rapid plasma displacement resulting from sudden pressure loss. It then gradually grows to the order of 10 MN at 30 ms as the vertical displacement increases and the plasma further contacts the simulation boundary. Then $\boldsymbol{F}_{\text{pl}}$ is approximately 20 MN vertically, and 200 kN sideways, in the end stage of the simulation, as shown in Fig. 6(a). In contrast, the vertical force exerting on the VV remains at a few MNs during both the TQ and VDE. Then the estimated $\boldsymbol{F}_{\text{vv}}$ is 2 MN vertically and 200 kN sideways at the end stage of the simulation, as shown in Fig. 6(b). The vertical forces of both $\boldsymbol{F}_{\text{pl}}$ and $\boldsymbol{F}_{\text{vv}}$ mainly originate from the symmetric component of the plasma and the VV currents. The vertical component of $\boldsymbol{F}_{\text{pl}}$ is directed upward, while that of $\boldsymbol{F}_{\text{vv}}$ is directed downward because the induced VV current flows in the opposite direction to the plasma current. Both the sideways forces are simultaneously excited by the plasma predominant asymmetric mode $m/n = 2/1$ growth after $t = 100$ ms, as shown in Fig. 6(d). After $t = 160$ ms, the instability becomes saturated, and the magnitudes of the two sideways forces stop growing. At this stage, the vertical component of $\boldsymbol{F}_{\text{vv}}$ is far less than that of $\boldsymbol{F}_{\text{pl}}$. This is consistent with the previous analysis that the current centroid has less displacement than the magnetic axis. Meanwhile, the magnitudes of the sideways components of $\boldsymbol{F}_{\text{vv}}$ and $\boldsymbol{F}_{\text{pl}}$ are in the same order of magnitude despite their phase difference. During the simulated CQ phase (from 30 ms to 220 ms), the plasma current inside the LCFS decreases from 8.1 MA to 6.5 MA and increases outside the LCFS from 4.2 MA to 6.0 MA, while the total plasma current remains approximately constant at 12.4 MA. Concurrently, the total induced current in the VV decreases from 2.16 MA to 1.65 MA. This shift

results in an increase in the vertical component of $\boldsymbol{F}_{\rm pl}$ due to the rising fraction of SOL current, whereas the decreasing current in the VV leads to a reduction in the vertical component of $\boldsymbol{F}_{\rm vv}$.

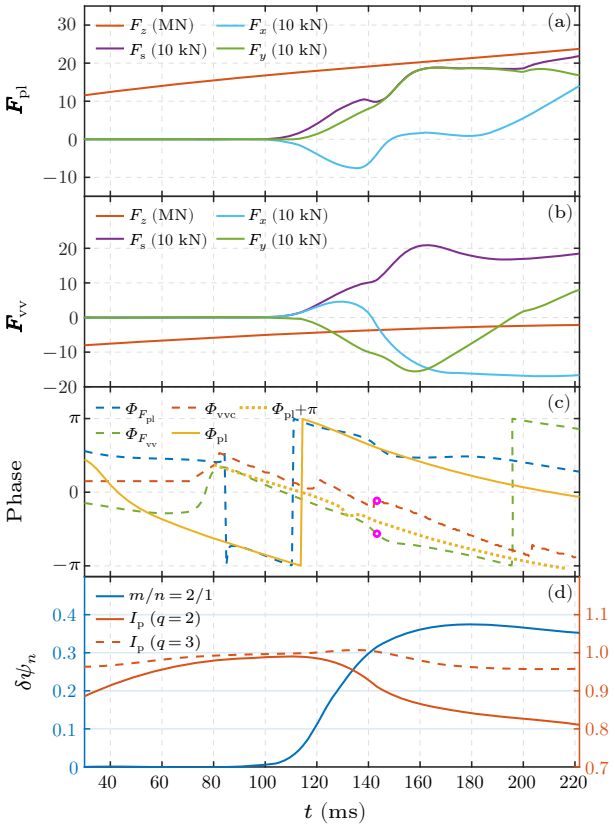

Fig. 6. Time evolution of the vertical (F_z) and sideways ($F_{\rm s}=\sqrt{F_x^2+F_y^2}$) forces encountered by (a) the plasma current and (b) the VV. (c) Time evolution of the sideways forces' toroidal phase of the plasma current $\Phi_{F_{\rm pl}}$ and the VV $\Phi_{F_{\rm vv}}$, together with the asymmetric VV current phase $\Phi_{\rm vvc}$ and the phase of the plasma perturbation $\Phi_{\rm pl}$. The magenta circles indicate the corresponding time in Fig. 5. (d) Time evolution of the magnitude of the dominant plasma mode with $m/n=2/1$ and the integrated current density inside the $q=2$ and $q=3$ surfaces.

The toroidal phases of $\Phi_{F_{\rm pl}}$ and $\Phi_{F_{\rm vv}}$ are defined as $\Phi=\arctan(F_y/F_x)$. In Fig. 6(c), $\Phi_{F_{\rm pl}}$ is found to always follow the magnetic island phase change $\Phi_{\rm pl}$, as can be seen by comparing the blue dashed line and the yellow solid line. Here the phase of plasma perturbation $\Phi_{\rm pl}$ is defined as the phase of the magnetic island of the mode $m/n=2/1$. The phase of the asymmetric component of the VV current $\Phi_{\rm vvc}$ is defined as the toroidal location of its maximum. As would be expected, $\Phi_{F_{\rm vv}}$ approximately keeps the same phase as $\Phi_{\rm vvc}$, while the asymmetric VV current phase $\Phi_{\rm vvc}$ approximately keeps the opposite phase with perturbed plasma phase $\Phi_{\rm pl}$. This is due to the fact that the induced VV current always tends to mirror the current perturbation within the VV. In general, the two sideways forces mentioned above point in different directions. Here the rotating frequency of the plasma instability mode, $\Phi_{\rm pl}$, is estimated to be -31.35 rad/s in the negative toroidal direction, averaged after $t=100$ ms. The rotating frequencies of the sideways components of the two forces are approximately the same as the plasma instability frequency. Figure 6(d) shows the integrated plasma currents within the $q=2$ and $q=3$ surfaces, normalized by the total plasma currents inside LCFS. The $I_{\rm p}$ inside the $q=2$ surface reaches its maximum at $t\approx 110$ ms when the growth rate of plasma mode $m/n=2/1$ is also maximized. This is consistent with the 2D current density profile distribution shown in Fig. 6(b). Afterward, potentially due to MHD-induced relaxation, the current portion within the $q=2$ surface decreases, and the 2/1 mode is also saturated as a result. The integrated plasma current inside the $q=1$ surface is small during the simulation. This explains why 1/1 kink mode, which can cause large sideways force, does not appear in our simulation. The calculated sideways force, utilizing the parameters of CFETR plasma along with the growth rate and rotation frequency of the dominant 2/1 mode, predicted by Eq. (33) in Ref. [32], is 173 kN, which matches the magnitude obtained in our simulation. The estimation of the ITER sideways force, extrapolated using the growth rate and rotation frequency of the CFETR plasma, is 595 kN, which does not exceed the previous maximal estimation of 3.2 MN.[6]

In summary, the first effort to analyze wall forces on CFETR during VDE has been conducted using the 3D reduced MHD code JOREK. The VDE occurs after a mimic thermal quench; the $m/n=2/1$ mode emerges as the dominant mode during the current quench phase as the plasma moves upwards and begins to scrape off against the simulation boundary, corresponding to the plasma-wall contact. The total force, $\boldsymbol{F}_{\rm tot}$, is estimated to be about 20 MN for the vertical force and about 250 kN for the sideways force. The pre-disruption plasma current is 11.2 MA and the toroidal magnetic field is 6.53 T. The sideways force is caused by both the asymmetric component of the induced current in the vacuum vessel and the SOL current in the open-field-line region of the plasma. These currents and the resulting sideways forces are closely associated with the dominant plasma mode in phase. The sideways EM force acting on the plasma SOL current keeps the same phase as the dominant plasma mode, and the sideways EM force acting on the vacuum vessel keeps the same phase as the asymmetric component of the vacuum vessel current, which, in turn, keeps the opposite phase to the dominant plasma mode. Such a strong correlation provides a possible way to control the phase of sideways force to minimize wall damage by controlling the mode phase in future fusion operations, not only for CFETR but also for other fusion devices. The limitation of this work is that we have only included the force caused by the induced current flowing within the vacuum vessel, as well as the SOL current. The actual current sharing between the plasma and the vacuum vessel is beyond the scope of this work and will be further pursued in our future work. One would expect such a shared current to mostly act on the first wall and the blanket module instead of the vacuum vessel. Nevertheless, our study demonstrated the close phase correlation between the induced vacuum vessel current, the SOL current, their respective sideways force, and the plasma mode, paving the way for further studies in the sideways

force control during VDEs for CFETR plasmas.

Acknowledgments. The authors thank Dr. L. Xue and the CFETR group for their help in constructing the CFETR equilibrium and setting up the wall–coil configurations. We also thank Dr. N. Schwarz and Dr. F. J. Artola for fruitful discussions. This work was supported by the National MCF Energy R&D Program of China (Grant Nos. 2019YFE03010001 and 2018YFE0311300). This work was carried out on the supercomputer Tianhe-3 operated by NSCC-TJ.

References

[1] Doyle E, Houlberg W, Kamada Y *et al.* 2007 *Nucl. Fusion* **47** S18
[2] de Vries P C, Johnson M F, Segui I, and JET EFDA Contributors 2009 *Nucl. Fusion* **49** 055011
[3] Zhuang G, Li G Q, Li J, Wan Y X, Liu Y, Wang X L, Song Y T, Chan V, Yang Q W, Wan B N, Duan X R, Fu P, and Xiao B J, and the CFETR Design Team 2019 *Nucl. Fusion* **59** 112010
[4] Riccardo V, Walker S, and Noll P 2000 *Fusion Eng. Des.* **47** 389
[5] Pustovitov V D, Rubinacci G, and Villone F 2021 *Nucl. Fusion* **61** 036018
[6] Mironov D V and Pustovitov V D 2017 *Phys. Plasmas* **24** 092508
[7] Sovinec C R and Bunkers K J 2019 *Plasma Phys. Control. Fusion* **61** 024003
[8] Abate D, Yanovskiy V, Bonotto M, Cordaro L, Marchiori G, Pigatto L, and Pustovitov V D 2023 *Nucl. Fusion* **63** 126025
[9] Artola F J, Lackner K, Huijsmans G T A, Hoelzl M, Nardon E, and Loarte A 2020 *Phys. Plasmas* **27** 032501
[10] Artola F J, Loarte A, Hoelzl M, Lehnen M, Schwarz N, and the JOREK Team 2022 *Nucl. Fusion* **62** 056023
[11] Xue L, Duan X R, Zheng G Y, Liu Y Q, Yan S L, Dokuka V V, Khayrutdinov R R, and Lukash V E 2015 *Chin. Phys. Lett.* **32** 065203
[12] Xue L, Zheng G Y, Duan X R, Liu Y Q, Hoang G T, Li J X, Dokuka V N, Lukash V E, and Khayrutdinov R R 2019 *Fusion Eng. Des.* **143** 48
[13] Strauss H R, Paccagnella R, and Breslau J 2010 *Phys. Plasmas* **17** 082505
[14] Khayrutdinov R R, Lukash V E, and Pustovitov V D 2016 *Plasma Phys. Control. Fusion* **58** 115012
[15] Pustovitov V D, Rubinacci G, and Villone F 2017 *Nucl. Fusion* **57** 126038
[16] Clauser C F, Jardin S C, and Ferraro N M 2019 *Nucl. Fusion* **59** 126037
[17] Yanovskiy V V, Isernia N, Pustovitov V D, Scalera V, Villone F, Hromadka J, Imrisek M, Havlicek J, Hron M, and Panek R 2021 *Nucl. Fusion* **61** 096016
[18] Gerasimov S N, Abreu P, Baruzzo M, Drozdov V, Dvornova A, Havlicek J, Hender T C, Hronova O, Kruezi U, Li X, Markovič T, Pánek R, Rubinacci G, Tsalas M, Ventre S, Villone F, Zakharov L E, and JET Contributors 2015 *Nucl. Fusion* **55** 113006
[19] Strauss H, Joffrin E, Riccardo V, Breslau J, Paccagnella R, Fu G Y, and JET Contributors 2020 *Phys. Plasmas* **27** 022508
[20] Gerasimov S N, Hender T C, Morris J, Riccardo V, Zakharov L E, and JET EFDA Contributors 2014 *Nucl. Fusion* **54** 073009
[21] Lei M, Liu Z, Wu Q, Liu S, and Wang M 2023 *Nucl. Fusion* **63** 126045
[22] Hender T C, Wesley J C, Bialek J *et al.* 2007 *Nucl. Fusion* **47** S128
[23] Schwarz N, Artola F J, Vannini F, Hoelzl M, Bernert M, Bock A, Driessen T, Dunne M, Giannone L, Heinrich P, de Marné P, Papp G, Pautasso G, Gerasimov S, the ASDEX Upgrade Team, JET Contributors, and Team the JOREK 2023 *Nucl. Fusion* **63** 126016
[24] Artola F J, Sovinec C R, Jardin S C, Hoelzl M, Krebs I, and Clauser C 2021 *Phys. Plasmas* **28** 052511
[25] Bandaru V, Hoelzl M, Reux C, Ficker O, Silburn S, Lehnen M, Eidietis N, JOREK Team, and JET Contributors 2021 *Plasma Phys. Control. Fusion* **63** 035024
[26] Hoelzl M, Huijsmans G, Pamela S *et al.* 2021 *Nucl. Fusion* **61** 065001
[27] Hölzl M, Merkel P, Huysmans G T A, Nardon E, Strumberger E, McAdams R, Chapman I, Günter S, and Lackner K 2012 *J. Phys.: Conf. Ser.* **401** 012010
[28] Merkel P and Strumberger E 2015 arXiv:1508.04911 [physics.plasm-ph]
[29] Craddock G G 1991 *Phys. Fluids B: Plasma Phys.* **3** 316
[30] Strauss H 2018 *Phys. Plasmas* **25** 020702
[31] Pustovitov V D 2015 *Nucl. Fusion* **55** 113032
[32] Pustovitov V D 2022 *Nucl. Fusion* **62** 026036